Research Article

Zhongxue Feng, Yuhua Zhang, Jun Tan*, Yuming Chen, Yiming Chen, Jianbo Li, Xianhua Chen, Kaihong Zheng, and Fusheng Pan

Large strain hardening of magnesium containing *in situ* nanoparticles

https://doi.org/10.1515/ntrev-2021-0074
received May 18, 2021; accepted August 21, 2021

Abstract: In this work, *in situ* magnesium-based composite composed of nanoscale magnesium oxide (MgO), prepared by spark plasma sintering, shows significant plasticity and high strain hardening. During the strain-hardening stage, the incremental work-hardening exponent shows drastic fluctuations due to the pile-up and release of dislocations. The dislocation pile-up at the interface makes it possible to form dislocation cells. Mixed dislocations can be generated within the cells surrounding the MgO particles, which can interact with the stress field and effectively hinder the movement of dislocations, leading to an increase in dislocation density. What is more, grain boundaries have higher elastic modulus and hardness, which may lead to the appearance of microcracks and eventually intergranular fractures. Our results may shed some light on understanding the role of MgO particles in influencing the mechanical properties of Mg alloys and Mg-based composites, especially in work hardening.

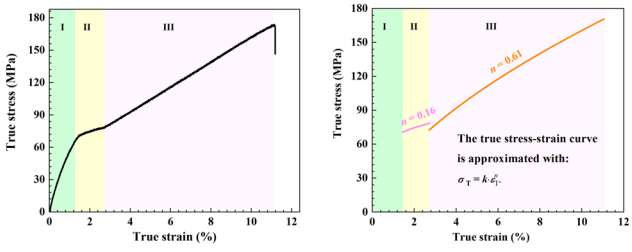

Graphical abstract

Keywords: nanoparticle, magnesium oxide, spark plasma sintering, work hardening, fracture behavior

1 Introduction

In general, the phenomenon of strain hardening (or work hardening) refers to the increase in strength and hardness of a material during plastic deformation below the recrystallization temperature (*e.g.*, room temperature), preventing further deformation of the material [1]. On the one hand, strain hardening can cause further machining difficulties for metal parts. However, its strain hardening can be eliminated by an intermediate annealing process [2]. On the other hand, it improves the strength [3,4], hardness [5,6], and wear resistance [7,8] of metals, which is particularly important for pure metals and certain alloys that cannot be strengthened by heat treatment [9]. Therefore, strain hardening can hinder the continued development of plastic deformation and greatly improve the safety of the components.

Magnesium (Mg) alloys and their composites are being actively developed and used in many applications, including the automobile, aircraft, and aerospace industries, because of their potential to improve energy efficiency [10–12]. However, the limited strength and stiffness of Mg alloys have restricted their large-scale application as structural materials [13–16]. As a result, Mg-based composites have been developed to improve the engineering strength and elastic modulus by adding reinforcements such as MgO [17], Al_2O_3 [18–20], SiC [21], TiC [22,23],

* **Corresponding author: Jun Tan,** National Engineering Research Center for Magnesium Alloys, Chongqing University, Chongqing 400044, China; College of Materials Science and Engineering, Chongqing University, Chongqing 400044, China, e-mail: tanjuncn@gmail.com, jun.tan@cqu.edu.cn
Zhongxue Feng: Faculty of Materials Science and Engineering, Kunming University of Science and Technology, Kunming 650093, China; National Engineering Research Center for Magnesium Alloys, Chongqing University, Chongqing 400044, China
Yuhua Zhang, Yuming Chen: Faculty of Materials Science and Engineering, Kunming University of Science and Technology, Kunming 650093, China
Yiming Chen: College of Materials Science and Engineering, Chongqing University, Chongqing 400044, China
Jianbo Li, Xianhua Chen, Fusheng Pan: National Engineering Research Center for Magnesium Alloys, Chongqing University, Chongqing 400044, China; College of Materials Science and Engineering, Chongqing University, Chongqing 400044, China
Kaihong Zheng: Institute of New Materials, Guangdong Academy of Sciences, Guangzhou 510650, China

TiO_2 [24], and CNTs [25–27]. Among them, MgO is almost inevitable in the preparation and processing of Mg alloys and Mg-based composites, although they are prepared in protective gas or even low vacuum. The excellent mechanical, physical, and thermal properties of MgO have been reported to make it a good candidate for the reinforcement of Mg-based composites [28].

Plastic deformation of materials containing hard nanoparticles generates internal stresses proportional to the applied plastic strain, which must be exceeded before further deformation can occur [29]. Then, strain hardening may occur due to dislocation movement and dislocation generation in the crystal structure of the material [30]. In a simple tension (uniaxial tensile test), strain hardening means only that the stress is a monotonically increasing function of the strain. The plastic deformation is then said to be stable [31]. The different weight percentages of Al_2O_3 nanoparticles in pure Mg and AZ31 affect the work-hardening behavior. The work-hardening capacity (WHC) varies from 0.05 to 1.07 [20]. It has also been reported that there was no significant strain hardening in the MgO/Mg composites prepared by disintegrated melt deposition method coupled with hot extrusion [32]. However, the distribution characteristics of MgO and the influence of the interface between MgO and Mg matrix on the mechanical behaviors, such as strain hardening and fracture behavior, are still elusive.

In the present study, *in situ* MgO/Mg composite is prepared by spark plasma sintering, and the mechanism of MgO influence on the mechanical properties and fracture behavior of the Mg matrix will be investigated in detail. Our results may be enlightening for understanding the role of MgO particles in influencing the mechanical properties of Mg alloys and Mg-based composites.

2 Experimental details

2.1 Materials

Mg powder with a purity of 99.8% was used for spark plasma sintering (SPS). The composition of the raw material is listed in Table 1. One can see that the Mg powder contains a small amount of Fe, Zn, and C. Figure 1 shows the morphology and powder size distribution of the Mg powder. All Mg particles are almost round with many small satellites around the larger particles as shown in Figures 1a and b. One can see that in Figure 1c and d, the particle sizes vary from 20 to 130 μm, and 90% of the Mg powder size is smaller than 94.0 ± 0.5 μm (D90, corresponding to 90% of the particle size of the cumulative size distribution of the sample, *i.e.*, 90% of the particles are smaller than it). The median size (D50) is about 60.5 ± 0.5 μm. The value of D10 is 36.6 ± 0.5 μm. The particles of different sizes were intentionally chosen in the hope of obtaining high densification during the sintering process. The size distribution is also fitted by Gaussian function, and the mean value of the particle size is 67.7 ± 0.9 μm with a high coefficient of determination (COD, R^2) of 96.3%.

Table 1: Chemical composition of Mg powders

Elements	Mg	Fe	Zn	C
Concentration (wt%)	99.81	0.008	0.008	0.004

2.2 SPS preparation

Mg powder was pre-pressed into a graphite mold (10 mm diameter) at a pressure of 15 MPa. It was then sintered with SPS at 853 K under argon (99.99%) atmosphere at a pressure of 35 MPa for 15 min.

2.3 Characterizations

The samples were machined, polished, and characterized to determine their microstructure and mechanical properties. The microstructure was investigated using scanning electron microscopy (SEM) and energy dispersive spectroscopy (EDS) techniques. Transmission electron microscopy (TEM) was also used to investigate the microstructure of the matrix and the interface between the Mg matrix and the MgO particles. Moreover, SEM and TEM were also used to analyze tensile fractography and failure behaviors. The elastic modulus and hardness were conducted by nano-indentation under the Nano-Blitz 3D mode at a constant force of 10 mN. The holding time was 1 s, the test was performed at a 30 × 30 array, and the interval between each adjacent test point was 5 μm to avoid mutual interference. Tensile tests were performed on specimens of 9 mm gauge, 2 mm width, and 1 mm thickness at a strain rate of $1 \times 10^{-3}\,s^{-1}$ at room temperature.

3 Results

3.1 Microstructures

Samples with a diameter of 10 mm and a height of about 20 mm were successfully sintered by SPS. SEM and TEM

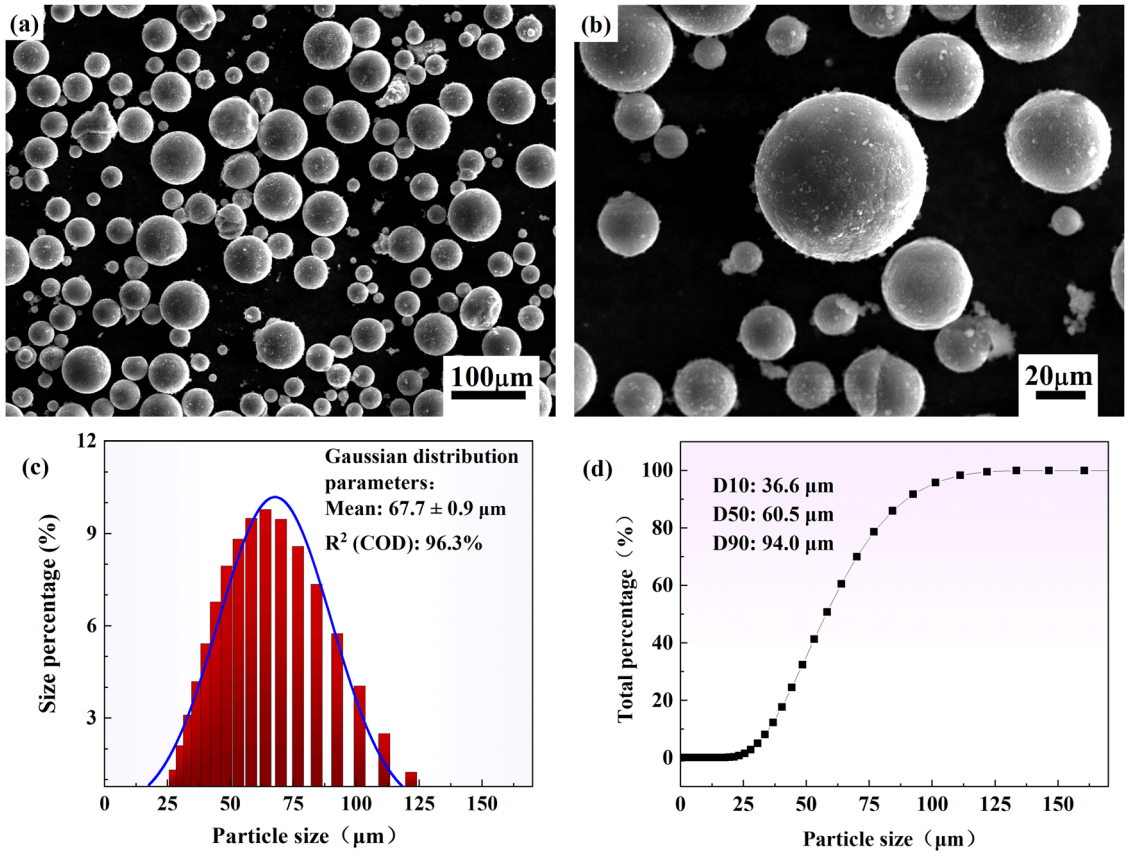

Figure 1: The morphology and the size distribution of Mg powders. (a) The macroscopic morphology of the particles. (b) An enlargement view of the particles showing that Mg particles are almost round with many small satellites around the larger particles. (c) The size distribution of Mg powders. The blue curve is fitted by Gaussian function and the corresponding mean value and standard error are shown in the inset. (d) The cumulative size percentage as a function of particle size.

were used to investigate the microstructure and the distribution of MgO (Figure 2). As can be seen in Figure 2a, a large number of fine MgO particles are concentrated near the particle boundaries. Figure 2b shows a magnified view. One can see that a very small amount of MgO particles is retained within the original Mg powder, as exemplified by some areas marked with red dotted lines. Moreover, the morphology of MgO particles near the grain boundaries was observed by TEM, illustrated in Figure 2c. Several different shapes can be observed, like sphericity, rod, and irregular shape. It is believed that there are two possible sources of MgO in this work. First, due to the chemical active nature of Mg, many MgO particles will inevitably be produced on the surface of powder during the powder preparation process. On the other hand, residual oxygen diffuses to form MgO particles despite the short sintering time of about 15 min required by the SPS process and the low vacuum environment. Since the nuclear of MgO depends mainly on the shape of the interface defects between the powders in SPS, the MgO shows various shapes in the Mg matrix, unlike the MgO in the melt, which relies only on the interface energy and forms a completely spherical shape. Figure 2d shows a high-resolution image of a MgO particle, and Figure 2e shows the inverse fast Fourier transform (IFFT) of the region marked with a blue rectangle in Figure 2d (marked with a blue “e”). According to the atomic stacking characteristics of MgO, we can distinguish the interface between MgO and matrix. As shown in Figure 2f, it has good interfacial adhesion between MgO and Mg matrix. Therefore, the *in situ* MgO/Mg composite is expected to obtain excellent mechanical properties.

The content and distribution of the MgO particle are of great importance to the mechanical properties of the MgO/Mg composite. First of all, the high-resolution SEM images were converted to black and white mode using open-source Python and OpenCV, which is a library of Python bindings designed to solve computer vision problems. The size distribution was then counted and shown in Figure 3. One can see that most sizes of MgO particles are of the order of a nanometer, ranging from several nanometers to ~250 nm. The percentage of the sizes

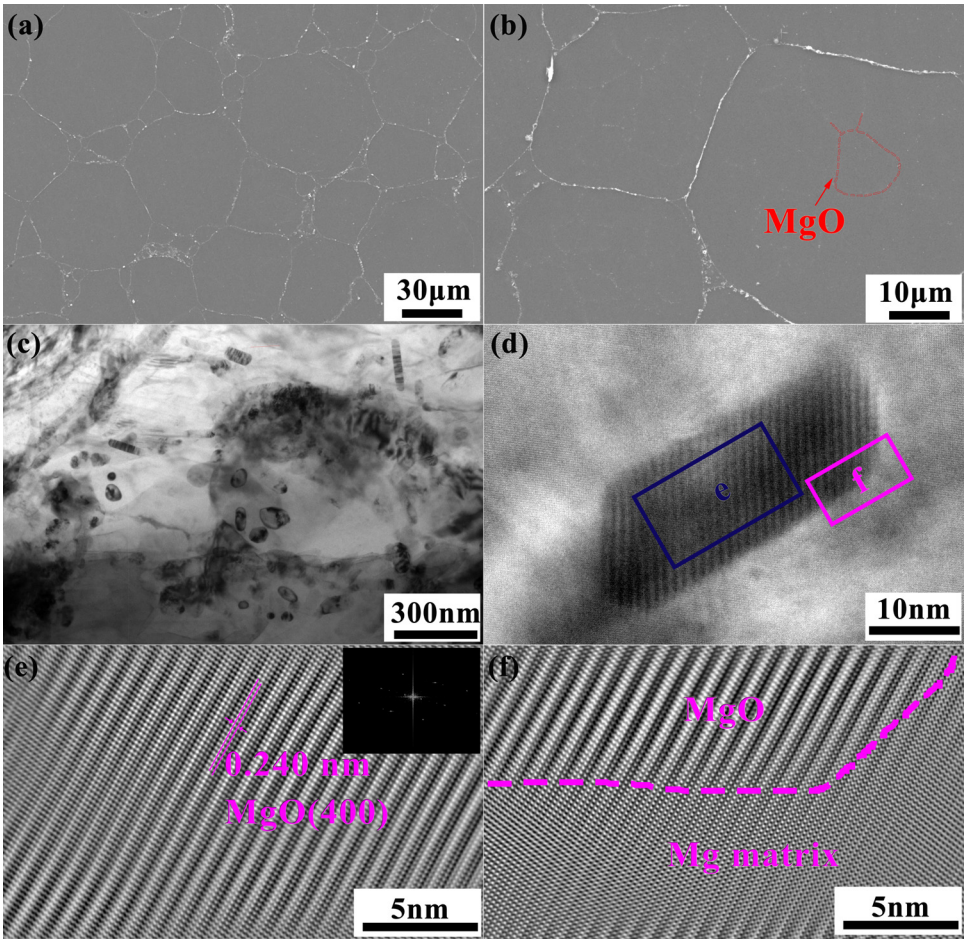

Figure 2: Microstructure of the as-sintered specimen. (a) SEM image of MgO/Mg composite prepared by spark plasma sintering. (b) A small amount of MgO particles were kept inside original Mg powders, marked with red dotted lines. (c) The morphology of MgO particles near the particle boundaries is sphericity, rod, and irregular shape. (d) High-resolution TEM image of the interface between MgO and Mg matrix. (e) An inverse fast Fourier transformation (IFFT) of the area marked with blue rectangle labeled with blue e in (d) and the inset shows the corresponding diffraction pattern. (f) An IFFT of the area marked with pink rectangle labeled with pink f in (d) indicating a good interfacial adhesion between MgO and Mg matrix.

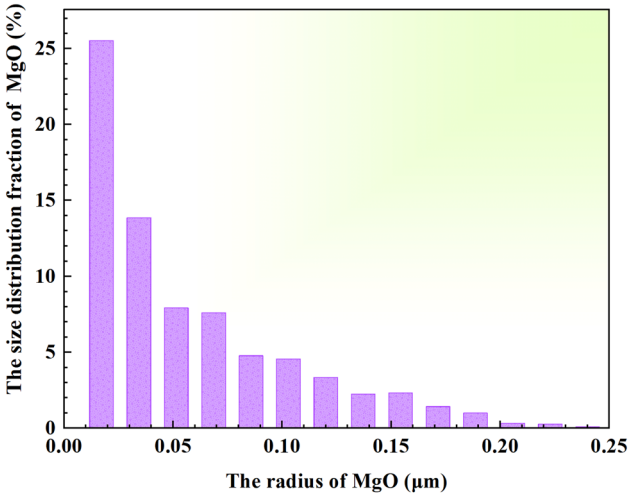

Figure 3: The size distribution of MgO particles in composite.

below 17 nm is 25.5%. The average particle size was about 22 ± 1 nm. The content of the MgO was 0.52 ± 0.08% calculated based on the area of the MgO particles.

3.2 The elastic modulus and hardness

Nanoindentation was used to investigate the elastic modulus and hardness around the interface of the Mg matrix in the Nano-Blitz 3D mode, which continuously measures the force and displacement over the entire area around the interface in constant steps (5 μm), making it possible to observe the evolution of the mechanical properties between the interface and the matrix (Figure 4). The relationship between the elastic modulus (E) and the indentation depth (h) can be described as follows [33]:

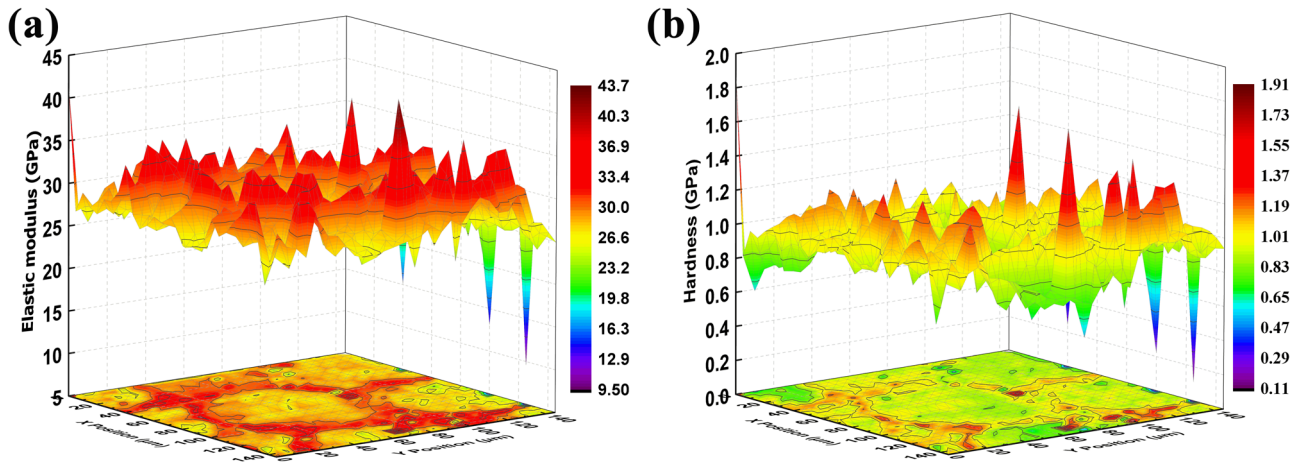

Figure 4: Three-dimensional graph and the corresponding contour map of the (a) elastic modulus and (b) hardness distribution of the specimen with an area of 150 μm × 150 μm.

$$E = \frac{\sqrt{\pi}}{2\sqrt{A}} \frac{\mathrm{d}P}{\mathrm{d}h}, \tag{1}$$

where E represents the elastic modulus and A represents the project area of the contact surface between the indenter and the matrix after the nanoindentation test. In the Berkovich triangular pyramid indenter, $A = 24.56h_c^2$ where h_c represents the vertical depth of the contact surface and $\mathrm{d}P/\mathrm{d}h$ represents the slope of the highest point of the unloading curve [34].

In Figure 4, a 3D plot of the elastic modulus and hardness of a sintered sample containing several Mg particles is shown. Significant changes of the elastic modulus and hardness are observed at the interface. The elastic modulus and hardness of the interface are higher than those of the Mg matrix, and the maximum values can reach 42 and 1.6 GPa, respectively. The average elastic modulus and hardness of the Mg matrix are only 27 and 0.85 GPa. Fortunately, the mechanical properties are continuous in the transition region between the interface and the matrix, which indicates that the bonding force is sufficient to improve the mechanical properties of the whole composite, which also suggests that there are no obvious defects between the MgO particles and the Mg matrix. And unlike the loose structure of the oxide layer in casting [35], in this work, by SPS, it has a good coherent interface between the MgO and the Mg matrix.

3.3 Tensile testing

The tensile engineering stress–strain curve of the MgO/Mg composite prepared by SPS is shown in Figure 5a. The tensile strength and elongation of Mg are 156 ± 2 MPa and 11 ± 1%, respectively. Based on the engineering stress–strain curve, the true stress–strain curve can be calculated as shown in Figure 5b.

To further analyze the evolution of the mechanical properties, the curve can be divided into three stages: elastic stage I, first strain-hardening stage II, and second strain-hardening stage III. This material exhibits a pronounced yield stage, which is different from other Mg-based composites, and it may be related to the dislocation pile-up at the interface. One can see that the yield strength (YS) and ultimate tensile strength (UTS) are 70 ± 2 and 170 ± 2 MPa, respectively. To our surprise, large strain hardening occurred in all replicate tests of *in situ* MgO/Mg composite prepared by SPS. However, *ex-situ* 1.0 vol% MgO/Mg composites prepared by the disintegrated melt deposition method coupled with hot extrusion had no significant strain-hardening stage investigated by Goh *et al.* [32]. The work-hardening capacity (WHC), defined as (UTS–YS)/YS, can be as high as 1.43, which is much higher than that of Mg-based composites reinforced by Al_2O_3, SiC, TiB_2, graphene nanoplatelets, graphene oxide, and so on [18–20,36–41].

4 Discussion

4.1 Strengthening mechanisms of the composite

Nanoparticles can improve the yield strength of the matrix of a composite [42,43]. The yield strength (σ_y) of our *in situ* MgO/Mg composite is associated with the

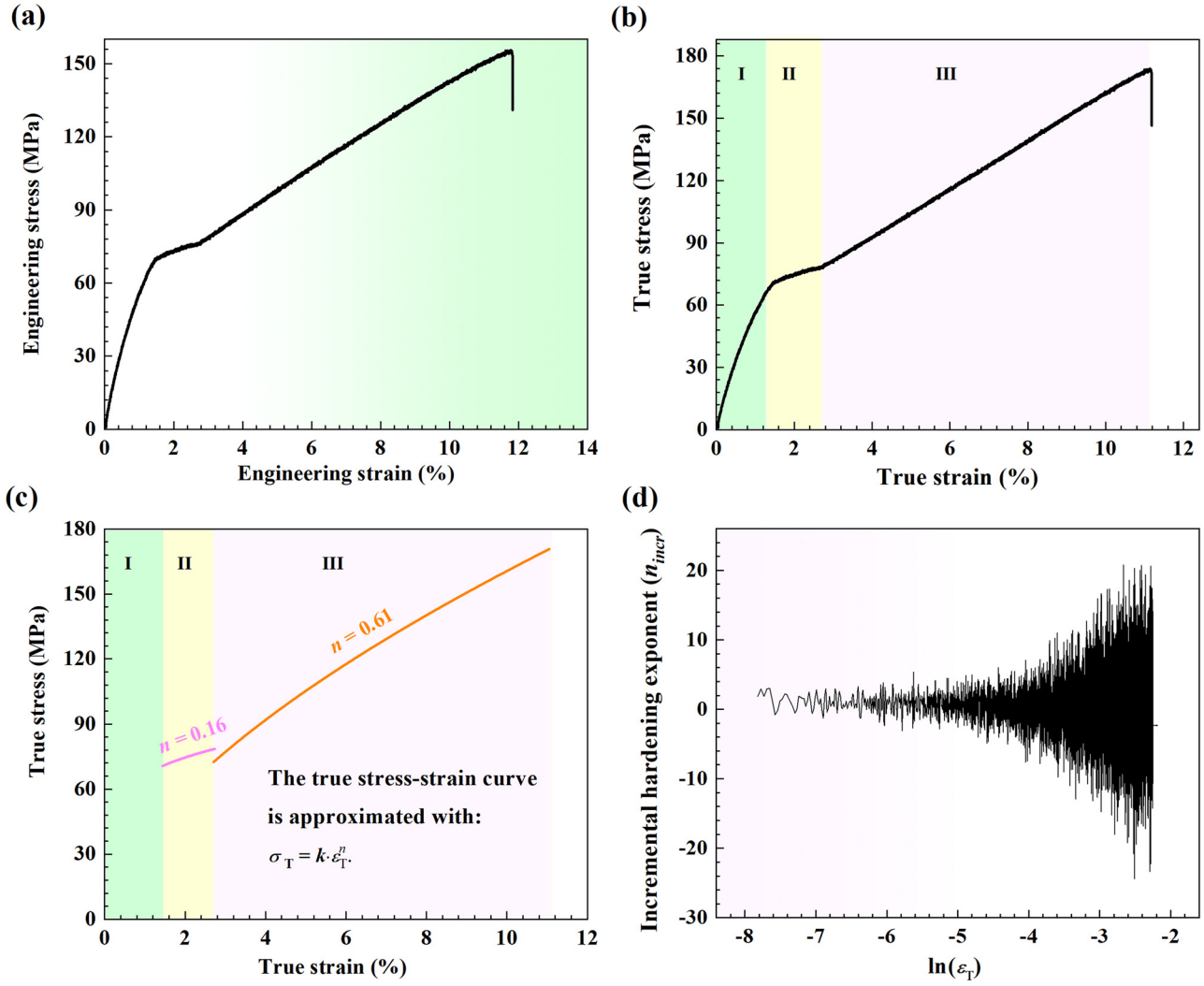

Figure 5: Tensile mechanical properties of the specimen at room temperature. (a) Engineering stress–strain curve and (b) true stress–strain curve of the specimen, which can be divided into three stages: elastic stage I, yield stage II, and strain-hardening stage III. (c) Strain-hardening exponent in different deformation stages. (d) Incremental-hardening exponent n_{incr} as a function of the natural logarithm of true strain ln(ε_T).

Hall–Petch effect [44,45], the Orowan strengthening mechanism ($\Delta\sigma_{Orowan}$) [46], and the modulus mismatch mechanism ($\Delta\sigma_{Modulus}$) [47]. Therefore, the quadratic summation method can be used to predict the yield strength [48]:

$$\sigma_y = \sigma_0 + k/d^{1/2} + (\Delta\sigma_{Orowan}{}^2 + \Delta\sigma_{Modulus}{}^2)^{1/2}, \quad (2)$$

where σ_0 is the friction stress when the dislocations slide on the slip plane, k is the stress concentration factor, and d is the size of the Mg matrix. The yield stress increases with decreasing d because pile-ups in the fine-grained material contain fewer dislocations, the stress at the tip of the pile-up decreases and, thus requiring a larger applied stress to generate dislocations in the adjacent grains [49,50]. During uniaxial tensile loading, MgO/Mg composites without following hot or cold deformation, like rolling and extrusion, have low friction stresses when dislocations slip on the slip plane [51].

Grain size has a profound effect on the value of k because it controls the original stress concentration generated by dislocation pile-up [52], and hence, the length of the dislocation acts on the dislocation sources in the adjacent grains [49]. Hence, σ_0 and k are set as 8.5 and 294 MPa μm$^{1/2}$, respectively [53], and the value of d can be obtained approximately from the Gaussian fitting parameter (67.7 μm) in Figure 1c. So, the contribution of

the grain refinement strengthening (Hall–Petch strengthening) is up to 44.2 MPa.

MgO particles hinder dislocation motion and leave a dislocation loop around them [54]; thus, the Orowan strengthening needs to be considered and $\Delta\sigma_{Orowan}$ can be roughly described by the Orowan–Ashby equation [46]:

$$\Delta\sigma_{Orowan} = \frac{0.13G_m b}{d_p\left[\left(\frac{1}{2V_p}\right)^{1/3} - 1\right]}\ln\left(\frac{d_p}{2b}\right), \quad (3)$$

where G_m is the shear modulus of the Mg matrix, b is the Burgers vector, d_p is the size of the MgO particles, and V_p is the volume percentage of the reinforcement. The following values were used to estimate the Orowan strength of the composite: G_m = 16.9 GPa [55] and b = 0.32 nm [32]. The value of the $\Delta\sigma_{Orowan}$ can be plotted according to different V_p and d_p, as shown in Figure 6. Therefore, one would expect an increase in $\Delta\sigma_{Orowan}$ for a higher volume percentage of the MgO particles (V_p) and smaller size of MgO particles (d_p). In this case, we set d_p = 22 nm and V_p = 0.52% based on the average of the statistical data in Figure 3. The contribution of the Orowan strengthening can reach 31.6 MPa.

In addition to grain refinement and Orowan mechanisms, the modulus mismatch strengthening mechanism can also improve the strength of composites. The modulus mismatch strengthening mechanism describes the generation of geometrically necessary dislocations when a composite is subjected to tensile loading. Because of the presence of MgO nanoparticle reinforcement, many geometrically necessary dislocations must be generated to accommodate the moduli difference between the matrix and the particles. Therefore, this modulus strengthening must be applied to the composite during tensile loading, and the strength improvement resulting from the modulus mismatch ($\Delta\sigma_{Modulus}$) can be calculated by ref. [48]

$$\Delta\sigma_{Modulus} = 3\alpha G_m\sqrt{2V_p\varepsilon b/d_p}, \quad (4)$$

where α is the material-specific coefficient, which is 0.5 for mixed dislocations [47]. ε is the strain of the composite, which is 0.2% for yield. So, the contribution of the modulus mismatch strengthen can only reach 12.2 MPa. However, the modulus mismatch strengthen can be further enhanced with increasing strain [56].

Consequently, the yield strength can be calculated by the quadratic summation method with a value of approximately 78.0 MPa, which is consistent with the yield strength value of 70 ± 2 MPa for the true stress–true stress curve. If the arithmetic summation method is used, which simply sums the contribution of the individual strengthening mechanisms in a linear fashion, the yield strength value is 88.0 MPa, which is slightly higher than that from the true stress–true stress curve, Therefore, the small size of the matrix, and high vol% of the reinforcement with small size favor higher yield strength for *in situ* MgO/Mg composite. It is noted that the size contribution of a matrix (Hall–Petch strengthening) is dominant in this work.

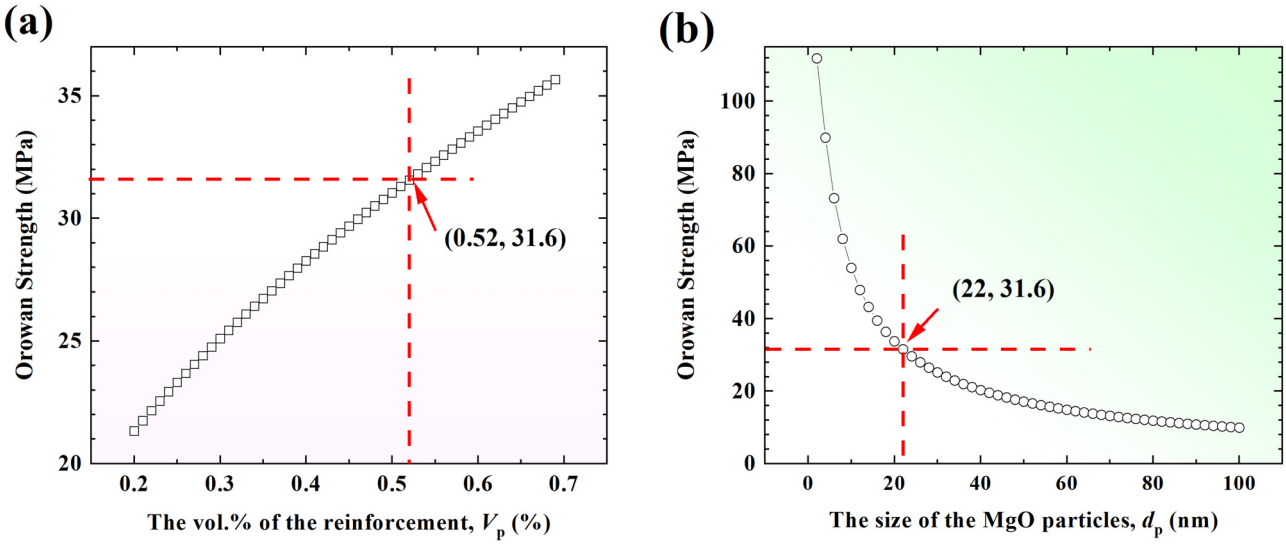

Figure 6: The Orowan strength as functions of (a) volume percentage (V_p) and (b) grain size (d_p) of reinforcement, respectively, implying a high Orowan strength lies in high vol% of the MgO particles and small grain size of MgO particles.

4.2 Origin of the strain hardening

The strain-hardening coefficient (or work-hardening index, n) can be obtained by fitting the uniaxial tensile curve with Holloman's equation and further quantifying the work-hardening effect. The Holloman's equation is a power–law relationship between the stress and the plastic strain and can be expressed as follows [57]:

$$\sigma_T = k\varepsilon_T^n, \tag{5}$$

where k is the strength coefficient. The value of n is between 0 and 1. $n = 0$ means that the material is a perfect plastic solid; while $n = 1$ represents a 100% elastic solid. Figure 5c shows the strain-hardening coefficient in different stage. Stage I is the elastic stage, so $n = 1$ (not shown here), stage II is the first strain-hardening stage and it is a transition of elastic deformation to elastic-plastic deformation stage with a strain-hardening coefficient of ~0.16, and stage III is the second strain-hardening stage with $n = 0.61$, which is larger than the coefficient of the previous stage. It can be concluded that in stage III, the homogeneous deformability increases with increasing strain [58]. Most metals have n values between 0.10 and 0.50, *i.e.*, the value of 0.61 exceeds that of most metals [59], *e.g.*, 4340 steel (tempered at 315°C, 0.12), AZ31B magnesium alloy (annealed, 0.16), 2024 aluminum alloy (T3 heat treatment, 0.17), low-carbon steel (annealed, 0.21), naval brass (annealed, 0.21), 304 stainless steel (annealed, 0.44), copper (annealed, 0.44), and transformation-induced work-hardening ZrCo alloy (0.51) [5].

Figure 5d presents the variation of the incremental work-hardening exponent (n_{incr}) as a function of the natural logarithm of true strain, *i.e.*, $\ln(\varepsilon_T)$, given by ref. [60]:

$$n_{\text{incr}} = \frac{d \ln \sigma_T}{d \ln \varepsilon_T}. \tag{6}$$

It is well known that the large homogeneous deformation of specimens is associated with a high, and slightly increasing n_{incr} during plastic deformation [60]. In our specimen, however, the value of n_{incr} fluctuates in the range of −20 to 20 and its amplitude is increasing with increasing strain until fracture, showing a trumpet-like shape. In comparison with other Mg-based composites, this specimen presents a completely different evolution of work hardening during plastic deformation. May it associate with the pile-ups and release behavior of dislocations?

Local shear stresses are necessary for the slip of dislocations. The density of dislocations will increase originally from the increasing local shear stresses, arising from three possible sources [61]:

- external loads and constraints,
- internal stress fields,
- or higher or lower compliance interaction interfaces.

In the tensile test of *in situ* MgO/Mg composite, the external loads come from the applied stress at both ends of the specimen. In addition, these stresses generate shear stresses at the level of the slip plane. In the dislocation theory of plasticity, the relation between the shear stress (τ) and the dislocation density (ρ) during the uniaxial tensile test can be expressed as

$$\tau = \alpha G_m b \rho^{1/2}, \tag{7}$$

where α is a constant at room temperature, G_m is the shear modulus of the Mg matrix, and b is the Burgers vector. Therefore, the ratio of the dislocation density is equal to the square ratio of the corresponding applied stress.

Internal stress fields can be generated by the microstructural features/influences of the MgO particles. These stresses can lead to certain shear stresses on the slip plane.

What's more, because of the different modulus between the Mg matrix and MgO particles, the interaction of the internal stress field with the interfaces can lead to the difference of the inherent stress field. There are three possible routines for the evolution of the dislocations [61]:

- A free surface will attract dislocations.
- When a moving dislocation slides over a soft coherent obstacle with a lower modulus, it will shear it. However, in our case, MgO particles are harder than the Mg matrix, so this is not possible.
- A dislocation can be pinned, thus hindering the dislocation motion. So, the dislocation has to bypass the pinned part under the applied stress. This leads to an increase in dislocation density.

To further explore the strain-hardening mechanism, the microstructure near the tensile fracture region was investigated by TEM. As shown in Figure 7, MgO particles, which gathered at the grain boundaries, could pin the dislocations, causing the dislocation lines to accumulate near the grain boundaries, and forming dislocation cells (Figure 7a). The cell walls exhibit a loose structure with thickness ranging from tens to hundreds of nanometers. After deducting the dislocation wall thickness, the inner width of the cell in our TEM image is estimated to be 720 nm and the dislocation cell concentrates at the grain boundaries. Due to the high density of the MgO particles around the grain boundaries, the glide of

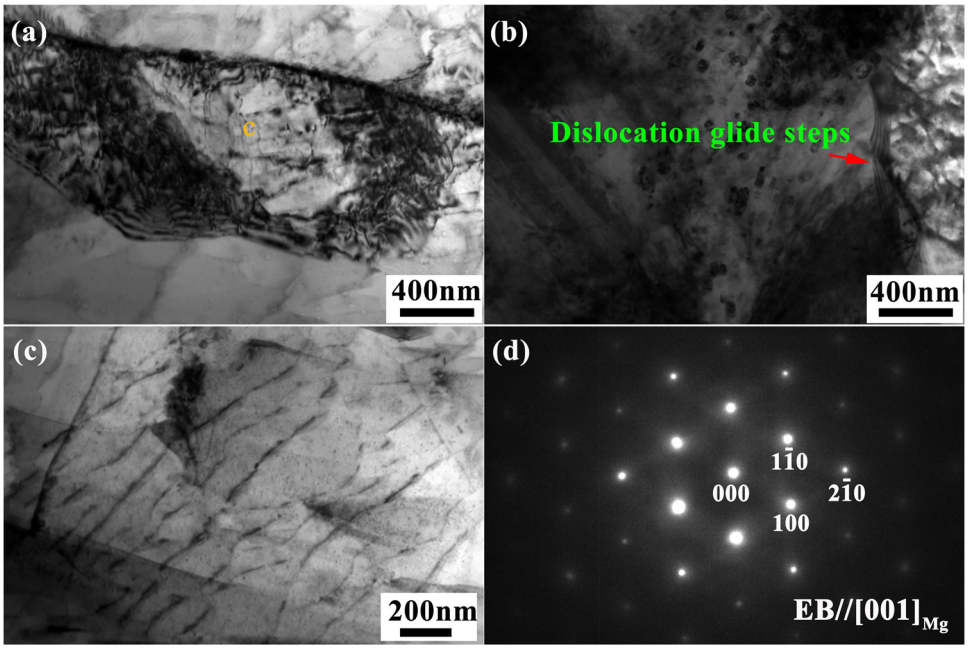

Figure 7: TEM images of the (a) dislocation cell and (b) dislocation glide steps in Mg sample. (c) A magnification view of the microstructure of the dislocation cell labeled with orange c in (a). (d) The corresponding diffraction pattern in (c).

dislocations through the climb and/or cross slip would be retarded or hampered (dislocation pile-ups) and n_{incr} would increase until new dislocations are restarted or pre-existing dislocation glide is accelerated. Then, dislocations will pile-up – release – pile-up – release. Finally, the dislocation glide steps will be formed and n_{incr} will be increased. The dislocation glide steps, marked with a red arrow, were observed and shown in Figure 7b. This shows that the dislocations are released at the interface. These dislocation behaviors may be responsible for the fluctuation of the increment strain-hardening exponent in *in situ* MgO/Mg composite prepared by SPS. The microstructure of the inner dislocation cell is displayed in Figure 7c. Many stacking faults are formed within the cell. To analyze whether the twining has occurred during the plastic deformation process, electron diffraction of the area *d* was tested [58]. The selected area diffraction pattern (SADP) is shown in Figure 7d, indicating the absence of twining within the dislocation walls.

The type of dislocation within the dislocation walls was distinguished by high-resolution TEM, as shown in Figure 8a. By comparing with the atomic model of the mixed dislocation shown in Figure 8b, the dislocation can be considered as a typical mixed dislocation located around the MgO particle. The interface is marked with red dots in Figure 8a. It is further verified that MgO can interact with the stress field, effectively hindering the movement of dislocation and leading to an increase in dislocation density.

4.3 Failure behaviors of the *in situ* MgO/Mg composite

To further investigate the failure behaviors of the composite, the fracture morphology after tensile testing at room temperature was observed by SEM, as illustrated in Figure 9a. The micro-fracture surface was characterized as "rock sugar," consisting of sharp edges and corners with a strong polyhedral feel, representing a typical intergranular fracture. In addition, many microcracks (marked by red arrows) can be found around the particle boundaries. In the present work, the microcracks start at the same position as the peak of the elastic modulus (Figure 9b). The reason can be explained as follows. The relationship between the volume strain (θ) and stress can be determined by the following formula:

$$\theta = \frac{3(1-2\mu)}{E}\frac{\sigma_1+\sigma_2+\sigma_3}{3}, \tag{8}$$

where μ denotes the Poisson's ratio, E is the elastic modulus, σ_1, σ_2, and σ_3 are three principal stresses, respectively. If $\sigma_m = \frac{\sigma_1+\sigma_2+\sigma_3}{3}$, equation (8) can be transformed into

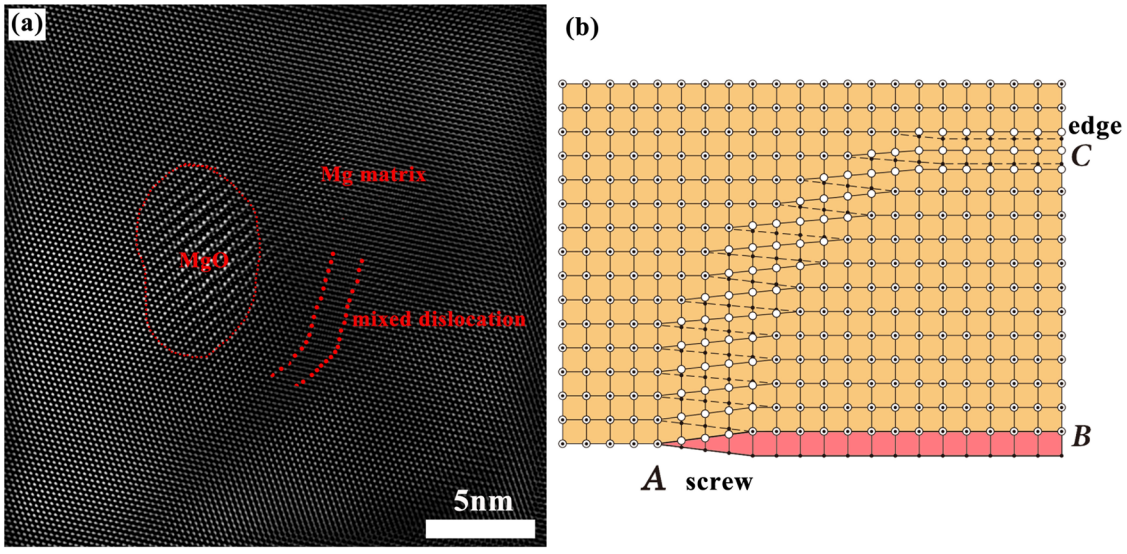

Figure 8: The interaction between dislocations and MgO particle. (a) A high resolution TEM IFFT image of mixed dislocation near MgO particle and (b) a atomic model of mixed dislocation.

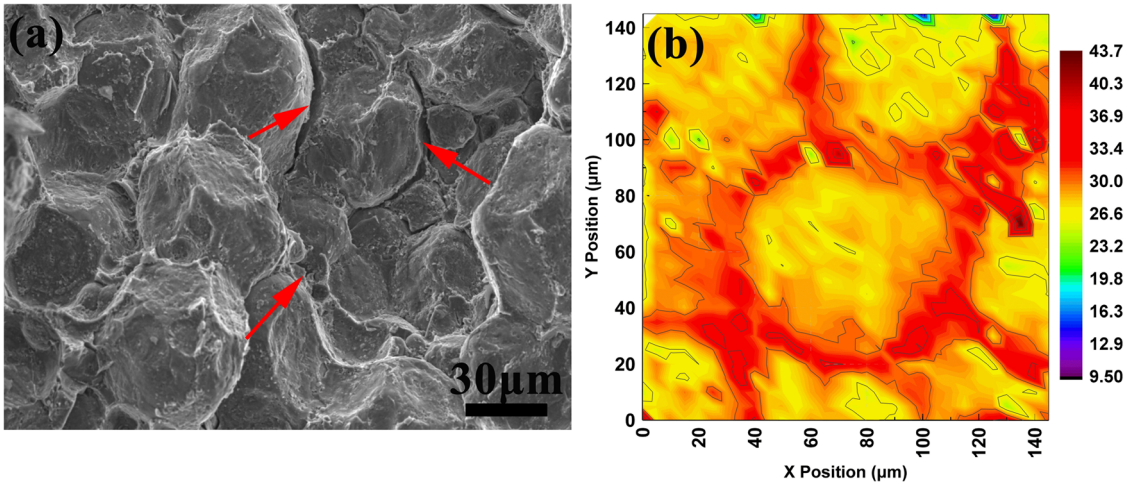

Figure 9: (a) Fracture morphology after tensile testing at room temperature and (b) the contour map of elastic modulus indicating that cracks originate at grain boundaries with higher elastic modulus marked with red arrows.

$$\theta = \frac{3(1-2\mu)}{E}\sigma_{\mathrm{m}}, \tag{9}$$

where μ_1 and μ_2 represent the Poisson's ratios of the matrix and the reinforcement, respectively. Under the same σ_{m}, the difference in the volume strains can be expressed by

$$\Delta\theta = \left[\frac{3(1-2\mu_1)}{E_{\mathrm{m}}} - \frac{3(1-2\mu_2)}{E_{\mathrm{p}}}\right]\sigma_{\mathrm{m}}. \tag{10}$$

Since the elastic modulus of the grain boundaries is much higher than that of the Mg matrix, the volume strain difference generated by the elastic modulus mismatch will increase considering the small variation of Poisson's ratio and elastic modulus of the matrix and reinforcement. As the grain boundaries contain a high density of misfit dislocations, it will produce microcracks, leading to stress concentration and eventually intergranular fracture during deformation.

5 Conclusion

In conclusion, *in situ* Mg-based composite composed of magnesium oxide (MgO) as reinforcement can be

prepared by using spark plasma sintering techniques. The results and discussion above allow the following conclusions:

(1) These MgO particles aggregated around grain boundaries can enhance strain hardening. These distribution characteristics lead to the pile-up of dislocations near the interface.
(2) A high strain-hardening coefficient (n = 0.61) can be obtained in a uniaxial tensile test, indicating an increase in uniform deformability with increasing strain. The n value of 0.61 exceeds that of most metals.
(3) MgO particles can interact with the stress field, effectively hindering the dislocation movement and leading to an increase in dislocation density.
(4) Considering the different values of elastic modulus between the interface and the matrix, it suggested that the interface may be a resource for cracks and eventually they lead to intergranular fractures.

Funding information: This work was supported by the Fund for Guangdong Major Project of Basic and Applied Basic Research (Grant No. 2020B0301030006), the Fundamental Research Funds for the Central Universities (2021CDJQY-040), Chongqing Special Project of Science and Technology Innovation of China (cstc2021yszx-jcyj0007), the National Natural Science Foundation of China (Grant No. 51861016), the Scientific Research Foundation of Department of Science and Technology, Yunnan (Grant No. 202001AT070041), and the open fund from the National Engineering Research Center for Magnesium Alloys (KKZ6201851008) as well as Henan Key Laboratory of Material Science and Technology (MDE2019-04).

Author contributions: All authors have accepted responsibility for the entire content of this manuscript and approved its submission.

Conflict of interest: The authors state no conflict of interest.

Data availability statement: The datasets generated during and/or analyzed during the current study are available from the corresponding author on reasonable request.

References

[1] Chen LY, Xu JQ, Choi H, Pozuelo M, Ma X, Bhowmick S, et al. Processing and properties of magnesium containing a dense uniform dispersion of nanoparticles. Nature. 2015;528(7583):539–43.
[2] Zhang Y, Jiang X, Sun H, Shao Z. Effect of annealing heat treatment on microstructure and mechanical properties of nonequiatomic CoCrFeNiMo medium-entropy alloys prepared by hot isostatic pressing. Nanotechnol Rev. 2020;9(1):580–95.
[3] Xu T, Yang Y, Peng X, Song J, Pan F. Overview of advancement and development trend on magnesium alloy. J Magnes Alloy. 2019;7(3):536–44.
[4] Wu G, Wang C, Sun M, Ding W. Recent developments and applications on high-performance cast magnesium rare-earth alloys. J Magnes Alloy. 2021;9(1):1–20.
[5] Li CJ, Tan J, Wang G, Bednarčík J, Zhu XK, Zhang Y, et al. Enhanced strength and transformation-induced plasticity in rapidly solidified Zr–Co–(Al) alloys. Scripta Mater. 2013;68(11):897–900.
[6] Chai Y, Song Y, Jiang B, Fu J, Jiang Z, Yang Q, et al. Comparison of microstructures and mechanical properties of composite extruded AZ31 sheets. J Magnes Alloy. 2019;7(4):545–54.
[7] Kocks UF, Mecking H. Physics and phenomenology of strain hardening: the FCC case. Prog Mater Sci. 2003;48(3):171–273.
[8] Carlton CE, Ferreira PJ. What is behind the inverse Hall-Petch effect in nanocrystalline materials? Acta Mater. 2007;55(11):3749–56.
[9] Kong L, Zhou Y, Song K, Hui D, Hu H, Guo B, et al. Effect of aging on properties and nanoscale precipitates of Cu-Ag-Cr alloy. Nanotechnol Rev. 2020;9(1):70–8.
[10] Xu W, Birbilis N, Sha G, Wang Y, Daniels JE, Xiao Y, et al. A high-specific-strength and corrosion-resistant magnesium alloy. Nat Mater. 2015;14(12):1229–35.
[11] Bommala VK, Krishna MG, Rao CT. Magnesium matrix composites for biomedical applications: a review. J Magnes Alloy. 2019;7(1):72–9.
[12] Atrens A, Shi ZM, Mehreen SU, Johnston S, Song GL, Chen XH, et al. Review of Mg alloy corrosion rates. J Magnes Alloy. 2020;8(4):989–98.
[13] Yu W, Li X, Vallet M, Tian L. High temperature damping behavior and dynamic Young's modulus of magnesium matrix composite reinforced by Ti_2AlC MAX phase particles. Mech Mater. 2019;129:246–53.
[14] Hassan SF, Ho KF, Gupta M. Increasing elastic modulus, strength and CTE of AZ91 by reinforcing pure magnesium with elemental copper. Mater Lett. 2004;58(16):2143–6.
[15] Song J, She J, Chen D, Pan F. Latest research advances on magnesium and magnesium alloys worldwide. J Magnes Alloy. 2020;8(1):1–41.
[16] Li S, Yang X, Hou J, Du W. A review on thermal conductivity of magnesium and its alloys. J Magnes Alloy. 2020;8(1):78–90.
[17] Zhang ZY, Guo YH, Zhao YT, Chen G, Wu JL, Liu MP. Effect of reinforcement spatial distribution on mechanical properties of MgO/ZK60 nanocomposites by powder metallurgy. Mater Charact. 2019;150:229–35.
[18] Hu M, Wei S, Shi Q, Ji Z, Xu H, Wang Y. Dynamic recrystallization behavior and mechanical properties of bimodal scale Al_2O_3 reinforced AZ31 composites by soild state synthesis. J Magnes Alloy. 2020;8(3):841–8.
[19] Chen Y, Guo Y, Gupta M, Shim V. A study of the dynamic compressive response of AZ31/Al_2O_3 nanocomposites and the influence of nanoparticles. Int J Impact Eng. 2016;89:114–23.

[20] Habibnejad-Korayem M, Mahmudi R, Poole WJ. Work hardening behavior of Mg-based nano-composites strengthened by Al_2O_3 nano-particles. Mater Sci Eng A-Struct. 2013;567:89–94.
[21] Rashad M, Pan F, Guo W, Lin H, Asif M, Irfan M. Effect of alumina and silicon carbide hybrid reinforcements on tensile, compressive and microhardness behavior of Mg–3Al–1Zn alloy. Mater Charact. 2015;106:382–9.
[22] Sahoo B, Panigrahi S. Synthesis characterization and mechanical properties of in situ (TiC-TiB_2) reinforced magnesium matrix composite. Mater Design. 2016;109:300–13.
[23] Anasori B, Barsoum MW. Energy damping in magnesium alloy composites reinforced with TiC or Ti_2AlC particles. Mater Sci Eng A-Struct. 2016;653:53–62.
[24] Meenashisundaram GK, Nai MH, Almajid A, Gupta M. Development of high performance Mg–TiO_2 nanocomposites targeting for biomedical/structural applications. Mater Design. 2015;65:104–14.
[25] Peigney A, Garcia FL, Estournès C, Weibel A, Laurent C. Toughening and hardening in double-walled carbon nanotube/nanostructured magnesia composites. Carbon. 2010;48(7):1952–60.
[26] Li H, Dai X, Zhao L, Li B, Wang H, Liang C, et al. Microstructure and properties of carbon nanotubes-reinforced magnesium matrix composites fabricated via novel in situ synthesis process. J Alloy Compd. 2019;785:146–55.
[27] Rashad M, Pan F, Asif M, Li L. Enhanced ductility of Mg–3Al–1Zn alloy reinforced with short length multi-walled carbon nanotubes using a powder metallurgy method. Prog Nat Sci. 2015;25(4):276–81.
[28] Wang Y, Fan Z, Zhou X, Thompson GE. Characterisation of magnesium oxide and its interface with α-Mg in Mg–Al-based alloys. Phil Mag Lett. 2011;91(8):516–29.
[29] Brown LM, Clarke DR. Work hardening due to internal stresses in composite materials. Acta Metall. 1975;23(7):821–30.
[30] Meyers MA, Mishra A, Benson DJ. Mechanical properties of nanocrystalline materials. Prog Mater Sci. 2006;51(4):427–556.
[31] Drucker DC. Some implications of work hardening and ideal plasticity. Q Appl Math. 1950;7(4):411–8.
[32] Goh CS, Gupta M, Wei J, Lee CL. Characterization of high performance Mg/MgO nanocomposites. J Compos Mater. 2007;41(19):2325–35.
[33] Sneddon IN. The relation between load and penetration in the axisymmetric Boussinesq problem for a punch of arbitrary profile. Int J Eng Sci. 1965;3(1):47–57.
[34] Li M, Tan J, Qin XM, Lu DH, Feng ZX, Li CJ, et al. Correlation between internal states and creep resistance in metallic glass thin films. J Appl Phys. 2021;129:8.
[35] Karakulak E. A review: past, present and future of grain refining of magnesium castings. J Magnes Alloy. 2019;7(3):355–69.
[36] Feng B, Feng XW, Yan CJ, Xin YC, Wang HY, Wang J, et al. On the rule of mixtures for bimetal composites without bonding. J Magnes Alloy. 2020;8(4):1253–61.
[37] Lee TJ, Kim WJ. Microstructure and tensile properties of magnesium nanocomposites fabricated using magnesium chips and carbon black. J Magnes Alloy. 2020;8(3):860–72.
[38] Meher A, Mahapatra MM, Samal P, Vundavilli PR. Study on effect of TiB_2 reinforcement on the microstructural and mechanical properties of magnesium RZ5 alloy based metal matrix composites. J Magnes Alloy. 2020;8(3):780–92.
[39] Munir K, Wen C, Li Y. Graphene nanoplatelets-reinforced magnesium metal matrix nanocomposites with superior mechanical and corrosion performance for biomedical applications. J Magnes Alloy. 2020;8(1):269–90.
[40] Tao J-X, Zhao M-C, Zhao Y-C, Yin D-F, Liu L, Gao C, et al. Influence of graphene oxide (GO) on microstructure and biodegradation of ZK30-xGO composites prepared by selective laser melting. J Magnes Alloy. 2020;8(3):952–62.
[41] Zhou P, Zhang S, Li M, Wang H, Cheng W, Wang L, et al. The creep behavior of Mg–9Al–1Si–1SiC composite at elevated temperature. J Magnes Alloy. 2020;8(3):944–51.
[42] Nie KB, Wang XJ, Deng KK, Hu XS, Wu K. Magnesium matrix composite reinforced by nanoparticles – a review. J Magnes Alloy. 2021;9(1):57–77.
[43] Wu Q, Miao WS, Zhang YD, Gao HJ, Hui D. Mechanical properties of nanomaterials: a review. Nanotechnol Rev. 2020;9(1):259–73.
[44] Hall EO. The deformation and ageing of mild steel: III discussion of results. Proc Phys Soc B. 1951;64(9):747–53.
[45] Petch NJ. The cleavage strength of polycrystals. J Iron Steel Inst. 1953;174:25–8.
[46] Zhang Z, Chen DL. Consideration of Orowan strengthening effect in particulate-reinforced metal matrix nanocomposites: a model for predicting their yield strength. Scripta Mater. 2006;54(7):1321–6.
[47] Dai LH, Ling Z, Bai YL. Size-dependent inelastic behavior of particle-reinforced metal–matrix composites. Compos Sci Technol. 2001;61(8):1057–63.
[48] Kim C-S, Sohn I, Nezafati M, Ferguson JB, Schultz BF, Bajestani-Gohari Z, et al. Prediction models for the yield strength of particle-reinforced unimodal pure magnesium (Mg) metal matrix nanocomposites (MMNCs). J Mater Sci. 2013;48(12):4191–204.
[49] Yu H, Xin Y, Wang M, Liu Q. Hall-Petch relationship in Mg alloys: a review. J Mater Sci Technol. 2018;34(2):248–56.
[50] Guan B, Xin Y, Huang X, Wu P, Liu Q. Quantitative prediction of texture effect on Hall–Petch slope for magnesium alloys. Acta Mater. 2019;173:142–52.
[51] Grishkov V, Kopylov V, Lotkov A, Latushkina S, Baturin A, Girsova N, et al. Effect of warm equal channel angular pressing on the structure and mechanical properties of Ti0.16Pd0.14Fe (wt%) alloy. Rev Adv Mater Sci. 2019;58(1):22–31.
[52] Bhaskar S, Kumar M, Patnaik A. Mechanical and Tribological overview of ceramic particulates reinforced aluminium alloy composites. Rev Adv Mater Sci. 2019;58(1):280–94.
[53] Somekawa H, Mukai T. Hall–Petch relation for deformation twinning in solid solution magnesium alloys. Mater Sci Eng A-Struct. 2013;561:378–85.
[54] Guan HD, Li CJ, Gao P, Yi JH, Bao R, Tao JM, et al. Fe-based metallic glass particles reinforced Al-7075 matrix composites prepared by spark plasma sintering. Adv Powder Technol. 2020;31(8):3500–6.
[55] Martienssen W, Warlimont H. Springer handbook of condensed matter and materials data. Berlin, Heidelberg: Springer; 2005.

[56] Ahmad SI, Hamoudi H, Abdala A, Ghouri ZK, Youssef KM. Graphene-reinforced bulk metal matrix composites: synthesis, microstructure, and properties. Rev Adv Mater Sci. 2020;59(1):67–114.
[57] Fischer FD, Reisner G, Werner E, Tanaka K, Cailletaud G, Antretter T. A new view on transformation induced plasticity (TRIP). Int J Plasticity. 2000;16(7–8):723–48.
[58] Liu T, Yang Q, Guo N, Lu Y, Song B. Stability of twins in Mg alloys – a short review. J Magnes Alloy. 2020;8(1):66–77.
[59] Callister Jr WD, Rethwisch DG. Fundamentals of materials science and engineering: an integrated approach. New Jersey, USA: John Wiley & Sons; 2020.
[60] Jacques PJ, Delannay F, Ladrière J. On the influence of interactions between phases on the mechanical stability of retained austenite in transformation-induced plasticity multiphase steels. Metall Mater Trans A. 2001;32:2759–68.
[61] Hull D, Bacon DJ. Introduction to dislocations. Amsterdam, Netherlands: Elsevier; 2011.